PHILOSOPHICAL TRANSACTIONS A

rsta.royalsocietypublishing.org

Research

Article submitted to journal

Subject Areas:
fluid mechanics, mechanical engineering

Keywords:
cavitation, nucleation, bubble dynamics, wavelets

Author for correspondence:
P. A. Brandner
P.Brandner@utas.edu.au

Wavelet analysis techniques in cavitating flows

Paul A. Brandner, James A. Venning and Bryce W. Pearce

Cavitation Research Laboratory
Australian Maritime College, University of Tasmania
Launceston, Tasmania 7250, Australia

Cavitating and bubbly flows involve a host of physical phenomena and processes ranging from nucleation, surface and interfacial effects, mass transfer via diffusion and phase change to macroscopic flow physics involving bubble dynamics, turbulent flow interactions and two-phase compressible effects. The complex physics that result from these phenomena and their interactions make for flows that are difficult to investigate and analyse. From an experimental perspective, evolving sensing technology and data processing provide opportunities for gaining new insight and understanding of these complex flows, and the continuous wavelet transform is a powerful tool to aid in their elucidation. Five case studies are presented involving many of these phenomena in which the continuous wavelet transform was key to data analysis and interpretation. A diverse set of experiments are presented involving a range of physical and temporal scales and experimental techniques. Bubble turbulent breakup is investigated using hydroacoustics, bubble dynamics and high-speed imaging; microbubbles are sized using light scattering and ultrasonic sensing; and large-scale coherent shedding driven by various mechanisms are analysed using simultaneous high-speed imaging and physical measurement techniques. The experimental setup, aspect of cavitation being addressed, how the wavelets were applied, their advantages over other techniques and key findings are presented for each case study.

This paper is part of a themed issue 'Redundancy Rules: The Continuous Wavelet Transform comes of Age'.

THE ROYAL SOCIETY PUBLISHING

1. Introduction

The use of wavelets generally in fluid mechanics has found diverse application in analysis [1] and simulation of turbulent single-phase flows [2]. The continuous wavelet transform (CWT) developed by Grossmann and Morlet [3] has been applied to the analysis of flows generally since the early 1990s, in common with its application in other fields of science and engineering. Fluid flows are characterised by temporospatial multi-scale chaotic, yet structured, features and phenomena, the understanding of which remains an ongoing challenge in many fields of research. As described in the early seminal works by Farge and Rabreau [4], Farge, et al. [5], Meneveau [6] and Farge [1] in the context of turbulent flows, wavelets provide the capability to resolve and analyse such coherent and intermittent features providing the opportunity for new insights into these intrinsic aspects of turbulence.

More recently, use of the CWT has found application in a broad range of flows including scale modulation and interaction in boundary layers [7,8], laminar to turbulent transition [9,10], unsteady pressure and acoustic field analyses [11–15] and vortex detection, evolution and bursting [16–19]. The continuous wavelet transform is advantageous over the classical Fourier transform (FT) for several reasons. In addition to the transient vs stationary aspects between the two methods [5], the FT is also susceptible to spuriously identifying the harmonics of frequencies required to build non-sinusoidal waves. This can be problematic, particularly in fluid mechanics applications, where harmonics can also be physical phenomena. For example, the transverse force of a bluff body oscillates at the Strouhal number, but the axial force changes at double the frequency [20]. It is therefore important to be able to identify when FT frequencies are either artifacts or are physically real, for which comparison with the CWT of the same data may be used.

Cavitating and bubbly flows by their multi-phase nature involve a range of physical phenomena and processes ranging from nucleation, surface and interfacial effects, mass transfer via diffusion and phase change to macroscopic flow physics involving, bubble dynamics, turbulent flow interactions and two-phase compressible effects. The complex physics that result from these phenomena and their interactions make for flows that are difficult to investigate and analyse. These difficulties and how they are approached experimentally are discussed in detail below.

The use of the CWT in the analysis of cavitating and bubbly flows has found broad application from classical cloud shedding physics [21–23], cavitation noise spectra [24,25], biomedical applications such as cavitation in mechanical heart valves [26], through to microbubble size measurement [27] and complex bubble dynamic behaviour [28,29]. Shedding cavitation may involve coherence with multiple frequencies present and frequency varying with flow conditions. Techniques for the analysis of such complex flows with varying spatial and temporal features, or ‘modes’, are extensively used for single-phase flow [30] and have also more recently begun to be applied in association with high-speed imaging of cavitating flow [31,32]. The CWT also has utility for identifying shedding modes in these two-phase flows, as described in section 6.

It has been found that differing wavelet forms [33] are more suited to identifying particular physical phenomena occurring in cavitating flows. In the example of cavitation about a jet in crossflow [34] there exists both highly periodic and aperiodic vortex systems for which a Morlet wavelet was used for analysis of the former, and a Degree of Gaussian-2 (DOG2) wavelet was more suitable to identify individual (aperiodic) shedding events. In the following discussion a number of examples are presented where the utility of the CWT in the analysis of cavitating and bubbly flows is discussed and illustrates some new insights gained into the underlying physics within flows that are inherently difficult to investigate.

2. Experimental modeling of hydrodynamic cavitation

Hydrodynamic cavitation is the change of phase from liquid to vapour that occurs when local pressures within moving or accelerated liquid volumes are reduced to, or below, vapour pressure. The inception of cavitation in practical liquid flows is invariably heterogeneous or at discrete sites of nucleation [35,36]. These sites, termed nuclei, are typically microbubbles or gas volumes trapped in microscopic crevices on surfaces. Nuclei are generated through various mechanisms such as mixing at free surfaces and liberation of dissolved gas present in practical liquid volumes. Typical background microbubble populations present in natural waterways range in diameter from $\mathcal{O}(1)$ to $\mathcal{O}(100)$ µm with concentrations from 0.01 to 10 cm^{-3} [37–40]. Populations generated by, for example, the disturbances created by ships produce much wider ranges of bubble sizes and concentrations.

Microbubble diameters increase or decrease as they are exposed to varying external pressures in a flow based on the balance of internal pressure with surface tension. The equilibrium of a microbubble is, however, only stable for a range of pressures such that below a critical value, dependent on bubble diameter and gas/vapour content, its equilibrium becomes unstable. Bubbles exposed to pressures at or below their critical pressure grow rapidly, essentially constrained only by the surrounding liquid inertia. Bubble critical pressures are below vapour pressure and mostly below absolute zero pressure such that in the absence of large nuclei liquids can sustain tensile stresses before inception occurs. Practically, for flows deplete of large nuclei, liquids may sustain several atmospheres of tension before inception. The liquid can be described as being in a state of metastable tension approximated by the Van der Waals equation [36]. The vapour pressure represents a state of dynamic equilibrium between a liquid and its vapour and is only an upper bound on the potential for vapour bubbles to form within the liquid.

The activation of a single nucleus or a large population may lead to the formation of quasi-steady or a diversity of highly unstable complex macroscopic cavitating flows involving a range of processes and phenomena, as noted above. Such flows associated with hydrodynamic devices and machinery create significant problems ranging from unsteady flow, loss of thrust or pressure, extreme vibration, noise, metal erosion and mechanical destruction. Cavitation may also be used for positive effects such as enhancing mixing and turbulent breakup [41], sterilisation [42], sonochemistry [43] through to noninvasive drug delivery and surgery [44].

The study of cavitation, as with other fluid phenomena, involves a large range of physical and temporal scales. Experimental investigation of nucleation and shockwaves generated in bubble dynamics involve sub-micron length scales and acquisition frequencies $\mathcal{O}(10)$ MHz. Whereas large scale phenomena involve metre length scales and time scales of seconds or longer. To investigate this range of phenomena various experimental capabilities have been developed in the Cavitation Research Laboratory (CRL) at the Australian Maritime College, the principal facility being a variable pressure water tunnel (figure 1). The tunnel test section is 0.6 m square by 2.6 m long in which the operating velocity and absolute pressure ranges are 2 to 12 m/s and 4 to 400 kPa, respectively. The tunnel volume is 365 m^3 with demineralised water as the working fluid. The tunnel has ancillaries for continuous injection and separation of microbubbles or large quantities of incondensable gas and for controlling the dissolved gas content. Microbubbles may be either injected for modeling cavitation nucleation or generated by the cavitation itself about experimental models. Microfluidic devices utilising cavitation at micron scales have been developed for generating high concentrations of microbubbles [45,46] (figure 1, bottom left). Arrays of these devices enable the test flow to be seeded with polydisperse nuclei populations with a dominant size of about 15 µm (figure 1, bottom right) to give concentrations in the water tunnel ranging from 0.1 to 100 $/\mathrm{cm}^3$.

Beyond the nuclei and dissolved content of the test water the primary non-dimensional quantities of interest in cavitation are the Reynolds number (Re) and the cavitation number (σ). The cavitation number reveals the likelihood and scale of any cavitation, and is defined as $\sigma = 2(p_\infty - p_v)/\rho U_\infty^2$ where p_∞ is the static pressure at the test-section centreline, p_v is the vapour pressure, ρ is the water density and U_∞ is the test-section velocity. The Reynolds

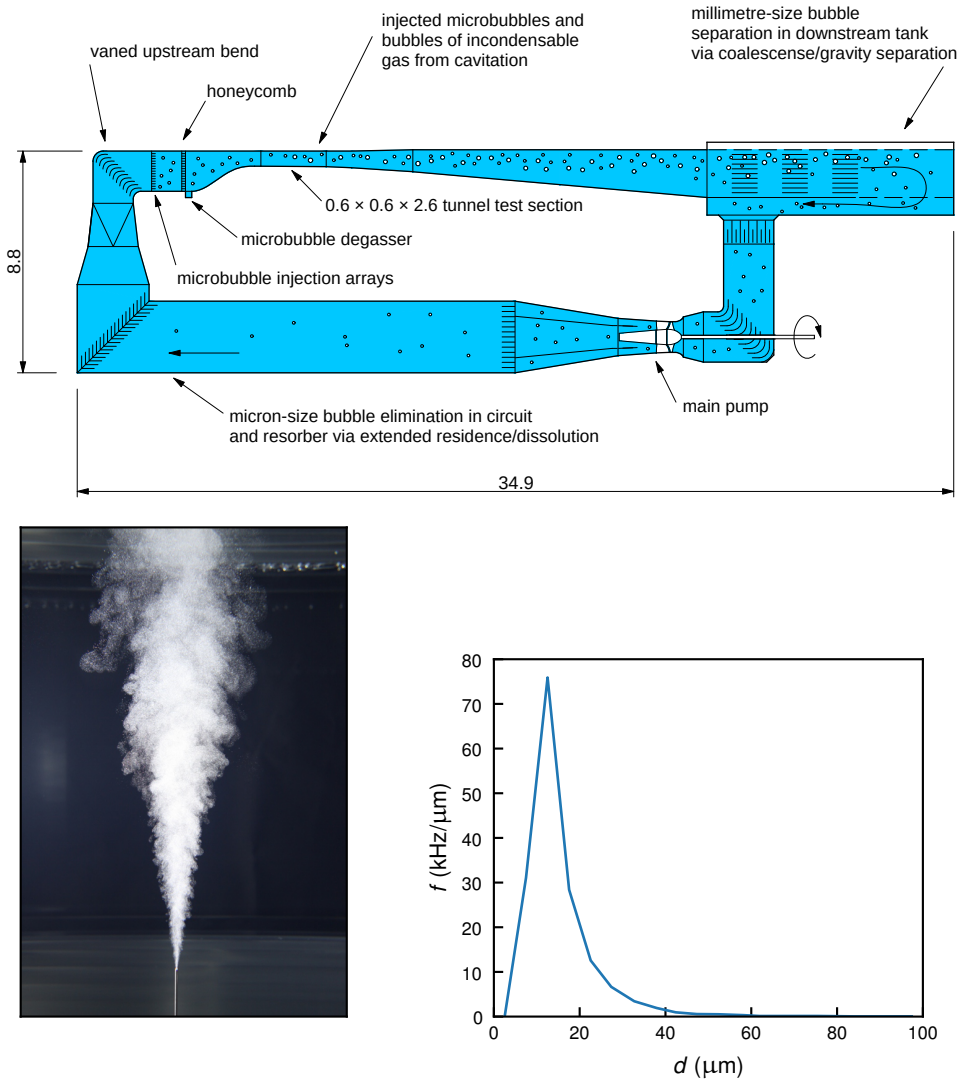

Figure 1. Schematic of the variable pressure water tunnel at AMC showing circuit architecture for continuous removal of microbubbles or large volumes of injected incondensable gas and ancillaries for microbubble seeding and for degassing of water. Microbubbles may be either injected for modeling cavitation nucleation or generated by the cavitation itself. All dimensions are in metres. Lower left: photograph of a polydisperse plume created by a microbubble injector. The plume has been measured with shadowgraphy and the histogram in terms of bubble production is in the lower right.

number is defined as $Re = U_\infty l/\nu$, where l is some relevant length scale, such as the chord of a hydrofoil, and ν is the kinematic viscosity of the water. Also of interest here is a pressure coefficient, defined as $C_p = 2(p - p_\infty)/\rho U_\infty^2$, where p is the local pressure and a lift coefficient, defined as $C_L = 2L/\rho U_\infty^2 cb$ where L is the lift force and c and b are the hydrofoil chord and span, respectively. Frequencies (f) are generally made non-dimensional by the Strouhal number, $St = fl/U_\infty$. Hydrofoil chordwise (x) and spanwise (z) positions are presented non-dimensionalised on the chord (x/c) and span (z/b), respectively.

Various experimental techniques have been developed in the CRL for investigating the aforementioned flows and range of phenomena for the majority of which the CWT has been applied. Perhaps the most valuable application of the CWT to cavitation is joint-time frequency

analysis of particularly short, but also long, time series data. All events in a data series can be identified using the CWT regardless of their nature. Coherent features vary from highly periodic to highly intermittent and typically non-sinusoidal. Classical Fourier analysis of such data doesn't provide the required temporal resolution and often results in nonphysical harmonic content being an artifact of the Fourier Transform. While the CWT has many advantages over classical Fourier analysis, in most cases the CWT has been found to not only provide new analysis techniques but also as a valuable complement to Fourier analysis in understanding temporal features that contribute to various spectral content. Several case studies are presented involving a range of applications in cavitating flows that highlight these advantages and how these capabilities have been used to gain new understanding of these fascinating but challenging flows.

3. Optical and mechanical measurement of cavitation nuclei

As discussed above, nuclei populations control the inception and dynamics of cavitation and are therefore critical for its rigorous modeling. Precise optical measurement of microbubbles or nuclei populations in hydrodynamic test facilities remains a challenge mainly due to the large working distances and the large range of concentrations and diameters involved. Direct imaging of bubbles, such as shadowgraphy, is limited in the range of concentrations it can measure, and the spatial domain of the measurement is limited by the smallest bubble of interest. To address these issues two additional techniques have been developed in the CRL, one being optical and the other mechanical. Neither of these techniques are recent but their development in the CRL relates to the use of contemporary equipment and analysis techniques including the CWT.

An illuminated bubble scatters light according to the Lorenz-Mie theory [47], which means the intensity of the scattered light varies with the viewing angle as illustrated in figure 2. The nature of this variation is a function of the refractive indices of the bubble and the surrounding medium, as well as the size of the bubble. As such, providing bubbles contain a similar consistency of gases, this angular intensity can be used as an effective means to size bubbles [48], which is referred to as Interferometric Mie Imaging (IMI). Figure 3 shows an out-of-focus photograph of two bubbles that are illuminated by a laser sheet. The two bubbles are different sizes, though the discs produced on the image plane are the same since this is only a function of the optical setup and the position of the bubble within the light sheet. The number or spacing of the fringes across each disc indicate the different sizes. Local maxima can be extracted from the scalogram to give the required fringe spacing. Given the few repetitions of the fringes (in some cases this can be as low as two), the FT is not necessarily well suited to this task.

For low concentrations of microbubbles that are too small for conventional imaging, nuclei can be mechanically activated and measured in a device known as a Cavitation Susceptibility Meter (CSM) [49]. This is a hydrodynamic device in which a venturi is deployed to reduce the pressure of a water sample activating any nuclei and therefore measuring the critical pressure of microbubbles or other active nuclei. Water is continuously sampled from the tunnel and passed through the venturi activating all nuclei with critical pressures below the throat pressure. These activations can be counted with ultrasonic sensing and the volumetric concentration is derived from the activation rate and the sampled flow rate. Bubble sizes can be derived from the venturi throat pressure and the equations for bubble equilibrium [50]. By incrementally reducing the throat pressure by flow rate increase, or static pressure reduction, a cumulative histogram of bubble size against concentration can be measured. This techniques allows nuclei with critical pressures equivalent to bubble sizes below 1 µm in diameter to be measured. There is no lower limit on the minimum concentrations that can be measured other than the length of time required to obtain converged statistics. However, it is limited by high concentrations as excessive activations can introduce errors into the counting procedure or saturate the venturi. As the test flow must be sampled, this method lacks spatial and temporal resolution and is only effective for flows with homogeneous nuclei distributions. These instruments have traditionally employed filtering techniques for counting the nuclei activations suitable for real-time operation however the CWT has been used to analyse signals and improve the measurement precision.

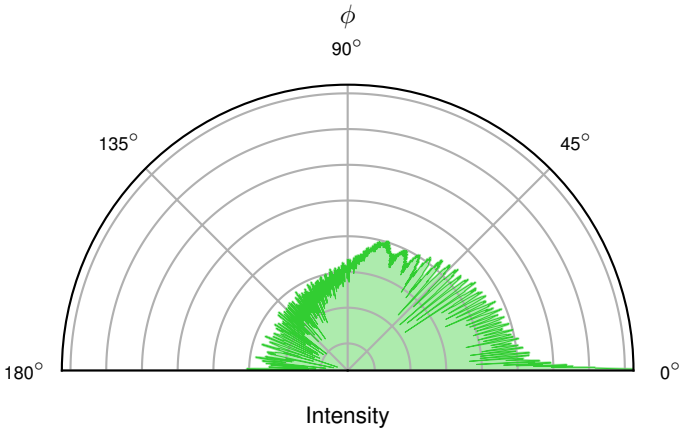

Figure 2. The intensity of scattered light as a function of the viewing angle for a 30 µm bubble in water illuminated by perpendicularly polarized 532 nm light.

A typical segment of the time series sampled from the output of a piezo-ceramic sensor attached to the CRL CSM is shown in the top plot of figure 4. For the time period shown several bubbles are activated. The data were sampled for this experiment at 2 MHz to resolve events lasting microseconds. There are several microbubble activations within the signal between $t = 0.02$ s and $t = 0.09$ s, manifesting as sharp spikes in the voltage output. The second plot in figure 4 is the signal after post-processing involving a series of filtering, rectification and homogenisation procedures currently used for CSM real-time operation [50]. The last two plots are the CWT scalogram and an integrated sample for the bandwidth indicated. The activation of a bubble causes a response at a wide range of frequencies due to the mechanical vibrations within the system, as shown in the CWT scalogram. It is the discretisation of these events that is the challenge in processing these signals, particularly given they may occur at rates of $\mathcal{O}(100)$ Hz with characteristic frequencies between $f = 2^{14}$ Hz and $f = 2^{18}$ Hz.

The CWT can be used to gain greater insight into the signal content to improve real-time detection algorithms or for post-processing of data. It has been used to find the relevant frequency bands and to optimise processing variables. It can also be used to improve algorithms for detection or discrimination of multiple activations. CWT analysis of the data have also shown intermittent pre-signals prior to the activation of single and multiple bubbles events which to date may be discriminated as a separate event. These events remain inexplicable and experiments involving simultaneous high-speed imaging with the ultrasonic sensing are planned to investigate these ambiguous events. While the CWT has been a valuable tool for ongoing development of these techniques it remains too computationally-expensive for real-time operation.

There exists a permanent background population within the CRL water tunnel [51]. These are of such low concentration and small size that they can only practically be measured with a CSM. A typical complete histogram of the background nuclei content in the CRL water tunnel, measured with a CSM, is given in figure 5. This measurement allows the determination of whether these nuclei are active in any particular experiment which is discussed further the case studies which follow.

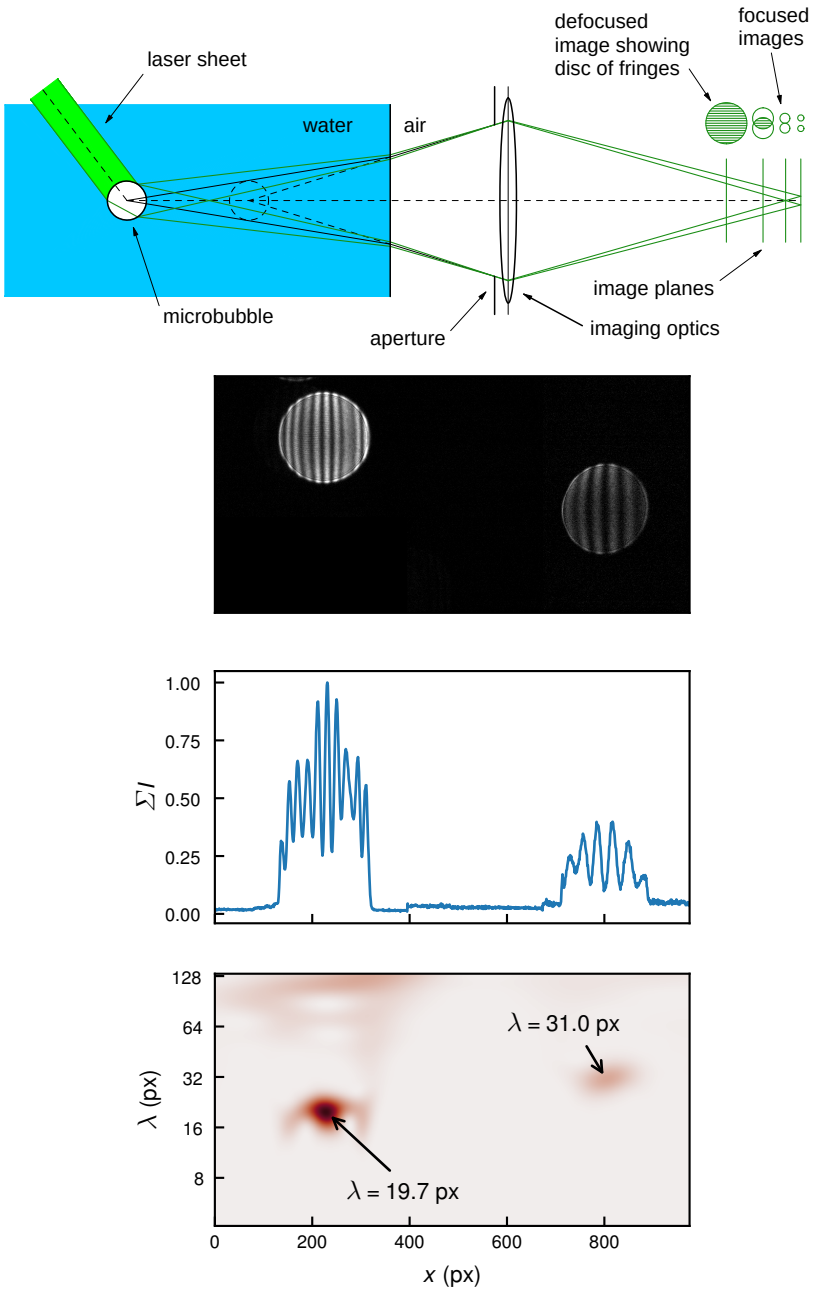

Figure 3. Use of wavelets to analyse fringe patterns obtained by Interferometric Mie Imaging of microbubbles. A schematic of the optical arrangement used (top) indicates how the raw image (second) was generated. The image shows the presence of two bubbles of different sizes, evidenced by the differing number of fringes. The third plot is the sum of pixel intensities down the image. The bottom figure is the magnitude of the Morlet wavelet transform across this signal ($|T(x,\lambda)|$), correctly identifying the fringe spacing (λ) for the two different sized bubbles.

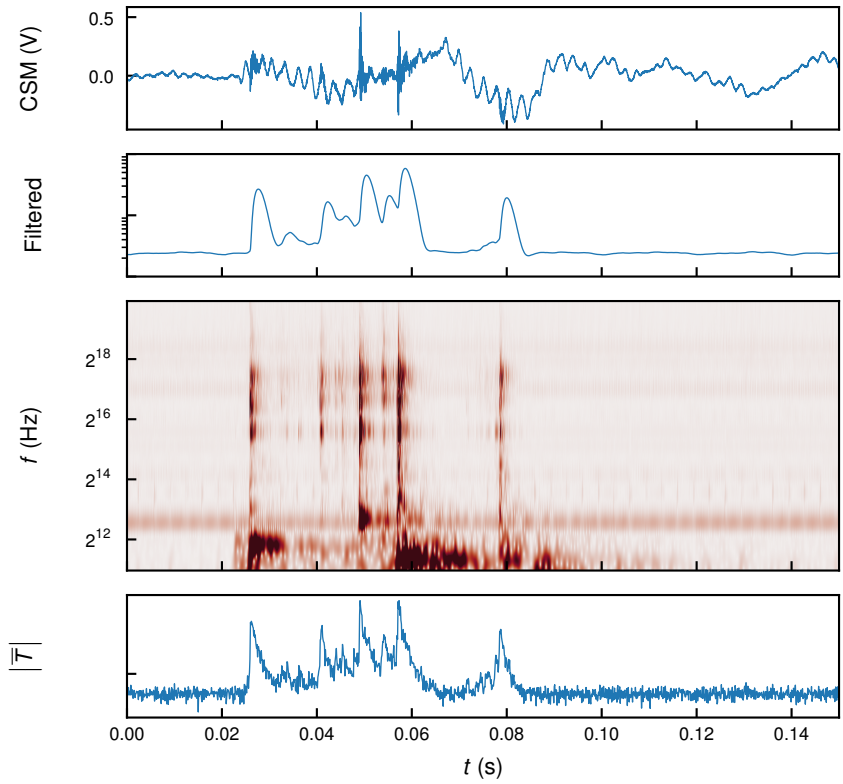

Figure 4. Time-series (top) from the CSM showing acoustic excitation events due to microbubble explosion, growth, and collapse. The second plot is the output of the filtering technique, showing the smoothing that occurs between consecutive events. The third plot is the CWT scalogram (absolute value using the Morlet wavelet). The bottom plot is a time-series of the mean wavelet power between $f = 2^{14}$ Hz and $f = 2^{18}$ Hz.

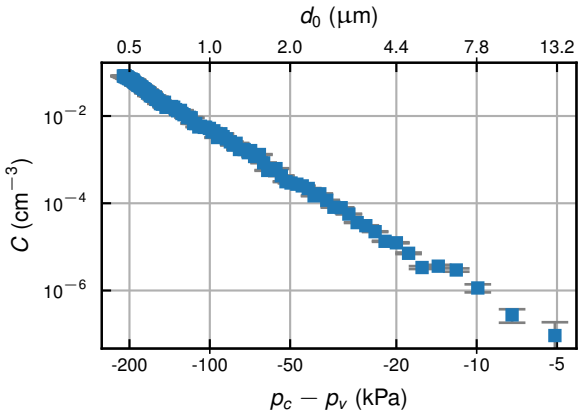

Figure 5. Cumulative background nuclei distribution in the AMC cavitation tunnel [51]. Nuclei concentration (C) is plotted against the water tension ($p_c - p_v$) where p_c is the critical pressure at which the nuclei are activated in the venturi throat. The secondary horizontal axis is the bubble size (d_0) in the tunnel test section associated with the critical pressure value.

4. Analysis of turbulent bubble breakup

As briefly noted above, microbubbles that provide cavitation nuclei are generated by wave action and through air ingestion and turbulent breakup. Also noted is that cavitation generates microbubbles upon condensation and turbulent breakup. Even though cavitation may only form and condense over short time scales typically this is sufficient time for dissolved incondensable gas in the surrounding liquid to diffuse, due to concentration gradient, into the vapour cavity. Upon condensation a mist of microbubbles of incondensable gas persists into the far wake, the population of which depends on the turbulent flows physics involved in the condensation/breakup and the incondensable gas flux. These flows are of interest in a range of disciplines in naval [52,53] and chemical engineering [54,55], and oceanography [56,57] for not only the physics of breakup and mass transfer but also aspects such as acoustic emissions [58,59].

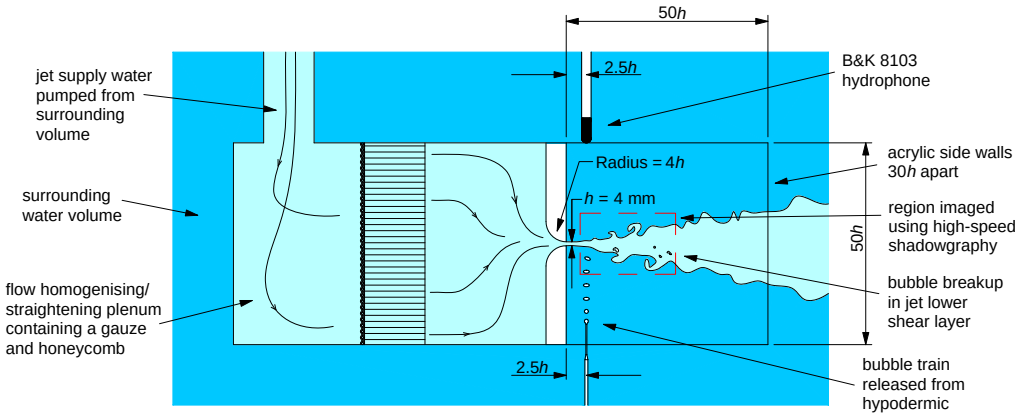

Figure 6. Schematic side view experimental setup for investigating breakup of millimeter bubbles in a turbulent shear layer. A plane jet is created between confining side walls in a surrounding water volume below which a bubble train is released. The bubble breakup is imaging using high-speed shadowgraphy and acoustic emissions recorded simultaneously with a hydrophone.

To model these processes in the laboratory an experiment involving breakup of millimetre-sized bubbles in a turbulent shear layer was developed in the CRL, shown schematically in figure 6. A train of nominally 3 mm diameter bubbles bubbles is released below a 4 mm thick plane jet in a tank of water (jet $Re = 4 \times 10^3$ based on jet thickness). The bubbles breakup as they rise and encounter the lower shear layer of the jet. The breakup is imaged using high-speed shadowgraphy (LaVision HighSpeedStar 8) sampled at 7 kHz and acoustic emissions are simultaneously recorded at 100 kHz using a hydrophone (Bruel and Kjaer model 8103). The acoustic measurements permit the detection of bubble excitation and breakup events that create noise and where breakup occurs the resulting products to be sized. Processing of the high-speed imaging provides information on bubble excitation and breakup products but not whether these produce noise. Sometimes, events can also be obscured for which the acoustic record provides additional information. The acoustic record of a bubble encountering the jet turbulent shear layer is ideally analysed using the CWT. Each event can be detected from the scalogram and any breakup products can be counted and sized as each bubble resonates at its natural frequency, from which, the bubble sizes can be derived using Minneart's equation or the Rayleigh-Plesset equation [35,60].

Sampled images from the high-speed shadowgraphy depicting the sequence of events typical of a bubble encounter with the jet shear layer are presented in figure 7. High-speed shadowgraphy of this bubble breakup and simultaneously recorded acoustic emissions are given in ESM1.These

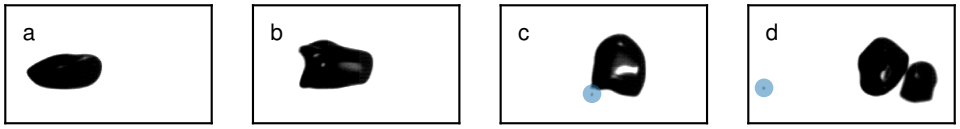

Figure 7. A sequence of photographs showing a single 3 mm bubble breaking up into three smaller bubbles with turbulence. Firstly (a-b) the bubble is stretched and deformed by the turbulence, (c) before releasing a 0.2 mm bubble (highlighted in blue). (d) The main bubble later splits into two bubbles (1.9 mm and 2.6 mm). The timing of the images is indicated by the grey vertical lines in figure 8.

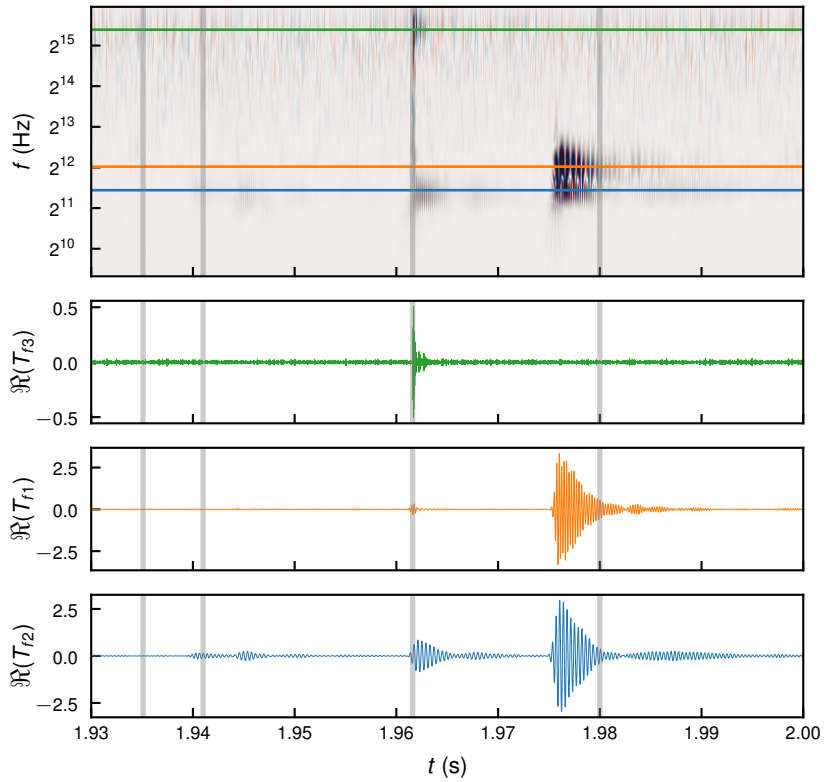

Figure 8. Real value of the Morlet wavelet transform of a hydrophone signal capturing the breakup of a bubble as it encounters a turbulent shear layer. The bottom three plots show the decaying oscillations of the bubble constituents, as slices through the wavelet data, for three different frequencies. These frequencies are proportional to the bubble size [60].

events include an initial distortion, a first breakup event and then a second. The corresponding CWT scalogram of the acoustic signal is shown in the top plot of figure 8. The natural frequencies of the 4 products are indicated by the colored horizontal lines in the scalogram. The vertical grey lines shown in figure 8 correspond to the images shown in figure 7. Image (a) shows the the undisturbed bubble just before it is about to encounter the shear layer and (b) shows the initial distortion that results in relatively weak acoustic emission. The distortion shown in (c) is sufficiently strong that a small bubble is separated, evident both on the scalogram and in the high-speed shadowgraphy. The last image (d) shows the separation of the large bubble into two further products as a final breakup event. This last event is evident temporally in the scalogram

Table 1. Comparison of bubble sizes determined optically by direct measurement from shadow imaging and calculated from the measured natural frequency of oscillation (obtained from CWT in figure 8) using Minneart's solution [60]

Diameter (imaging)	Measured frequency	Minneart's solution
0.2 mm	42.9 kHz ($2^{15.4}$ Hz)	0.2 mm
1.9 mm	4.2 kHz ($2^{12.0}$ Hz)	1.6 mm
2.6 mm	2.8 kHz ($2^{11.4}$ Hz)	2.5 mm

but not in the shadowgraphy as one of the bubble products optically obscures the other at initial separation. In each case the frequencies were used to size the breakup products and these closely match those determined directly from the imaging (table 1).

5. The influence of nucleation on cloud cavitation about a hydrofoil

As discussed above, nuclei populations control the inception and dynamic behavior of cavitation. These effects are fundamental to the operation of all hydrodynamic turbo-machinery and other devices involving lifting surfaces such as pump impellers, propellers and control surfaces. Basic research into cavitation physics related to such devices is often performed using canonical hydrofoil models being close representations of actual prototypes or generic analogies of blades of rotating machinery. To investigate the effects of nuclei on the classical problem of cloud cavitation, a simple hydrofoil geometry was developed for experiments in either nuclei deplete or nuclei abundant conditions representing two extremes of seeding that can occur in real flows. The CWT is a valuable tool in analyzing the spectral content and shedding modes of cloud cavitation for which examples are presented.

An anodised aluminium hydrofoil with a rectangular planform of 0.3 m span (b) and 0.15 m chord (c) with constant NACA-0015 section and a faired tip was mounted vertically from the water tunnel test-section ceiling via a 6-component force balance for dynamic force measurement simultaneous with high-speed imaging of the cavitation [61]. Measurements were made at fixed values of $\sigma = 0.55$, $Re = 1.4 \times 10^6$ (based on chord length), dissolved $O_2 = 3.3$ ppm and hydrofoil incidence of 6°. For the deplete case no nuclei are injected such that only background nuclei are present in the tunnel water. These have been measured using a CSM as described above (figure 5), from which it can be shown that they do not provide active nuclei in the freestream for this condition beyond inception. For the abundant case poly-disperse nuclei with a dominant size of about 25 μm are injected at a concentration of about 100 cm^{-3} [45]. This volumetric concentration results in an area concentration of activated nuclei of approximately 1 nuclei cm^{-2} on the hydrofoil. Simultaneous forces and high-speed images were recorded at 7 kHz for 3 s. Additional long-time series measurements of the forces for obtaining high-resolution spectra were recorded at 1 kHz for 240 s giving about 5,000 cycles of the dominant frequency.

Still images showing the cavitation about the hydrofoil for the nuclei deplete and nuclei abundant cases are shown in figure 9. Samples of the high-speed photography of each seeding case are given in ESM2 and ESM3. These provide an indication of the dramatic effect changes in nucleation have on the cavitation physics for otherwise identical flow conditions. Observations of the high-speed imaging show the shedding mechanisms and frequency content are significantly altered [61]. A single line of pixels was extracted from high-speed photography and plotted in time to provide space-time plots that may be used in conjunction with CWT scalograms to analyse shedding phenomena. Both spanwise and chordwise space-time plots have been extracted for comparison with corresponding CWT scalograms as discussed below.

CWT scalograms of long time-series lift measurement using the Morlet wavelet and the resulting PSDs, as well as those from the Welch estimate for each seeding case are shown in

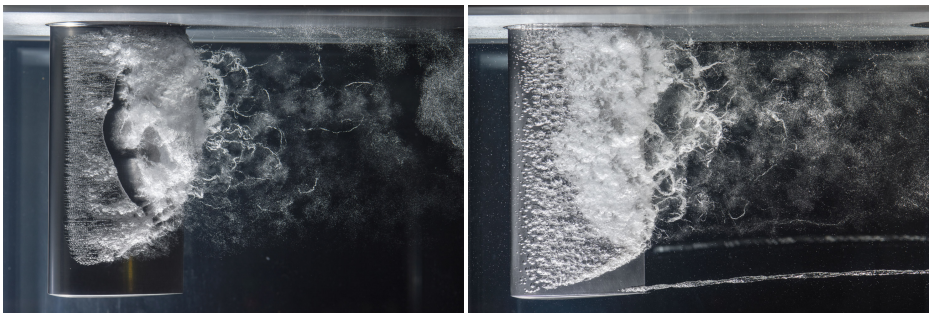

Figure 9. Photographs of cavitation about a foil for two different seeding conditions. On the left, no additional nuclei are supplied in the freestream, while on the right there is an abundance of weak nuclei that are continually activated.

figure 10. The usable frequency range of the balance is for about $St < 1$ beyond which force-balance response is evident. A series of well defined peaks are evident in the Welch PSD for both the nuclei-deplete and nuclei-abundant cases, where those from the CWT show fewer, less-defined peaks. For the nuclei-deplete case the CWT PSD shows three peaks below $St = 1$ which match with those in the Welch PSD. For the nuclei-abundant case the CWT PSD shows only two peaks, showing that the additional ones in the Welch PSD are harmonic artifacts of the FT. Examination of the data time-series and high-speed imaging provide conclusions that concur with these observations.

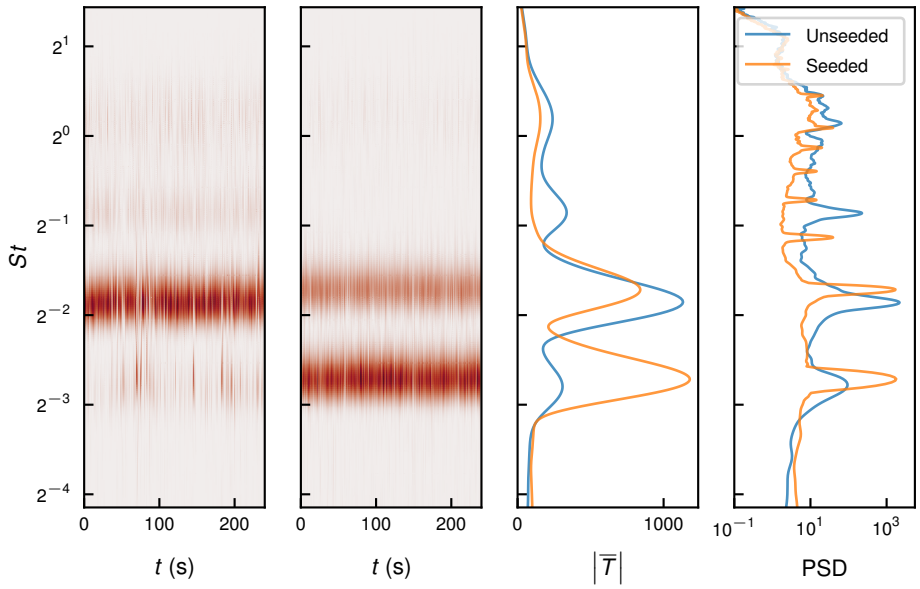

Figure 10. (from left) Absolute value of the Morlet wavelet transform on the lift signal for the cavitating foil without (first) and with (second) additional seeding. The time-average of the transforms are given in the third figure showing the frequency shift with the addition of seeding. The FTs are given in the right-hand figure.

A sample time series of the unsteady lift for the nuclei-deplete case is shown in the top plot of figure 11. In this case, the high-speed imaging (shown as chordwise and spanwise space-time plots) and force measurements show the dominant or fundamental frequency to be about

$St = 0.28$, which is the largest peak from the PSD. Frequency analysis of the high-speed imaging show this frequency to be associated with shedding involving large-scale cavity growth and collapse/condensation. Large-scale in this case refers to shedding involving cavity growth over almost the full chord. This fundamental frequency is evident in both the CWT scalogram and in both chordwise and spanwise space-time plots.

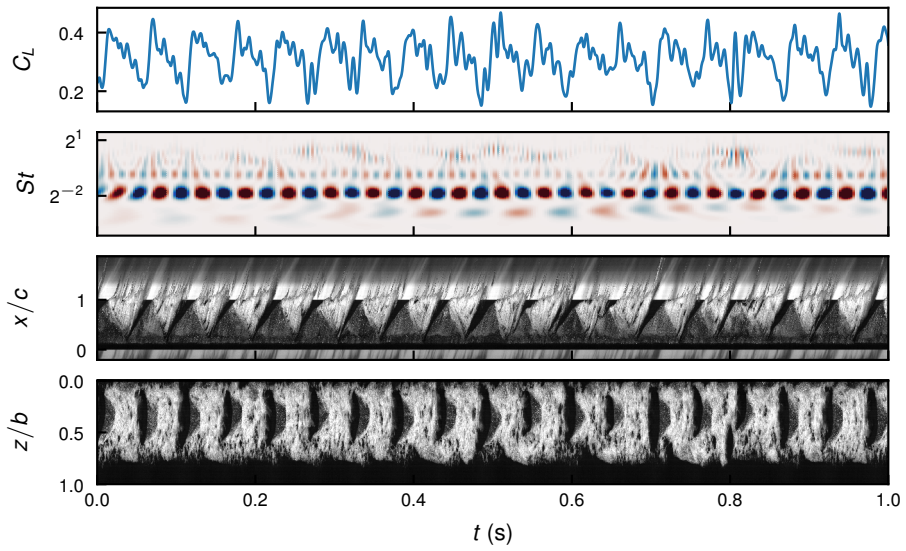

Figure 11. Wavelet analysis of a cavitating hydrofoil (nuclei deplete flow). The top row is the time history of the lift signal. The second figure is the real value of the Morlet wavelet transform. The bottom two figures are space-time plots at $z/b = \frac{1}{2}$ and $x/c = \frac{5}{6}$ respectively, showing the cavity extent as it varies in time.

The first frequency peak at about $St = 0.14$ can be shown to be associated with local shedding from the cavity end near the hydrofoil tip. It is a sub-harmonic of the fundamental and from the image analysis it can be shown that the local tip shedding varies at half the frequency of the bulk cavity shedding. That is, there are two separate but coupled shedding regions through the midspan and near the tip. This phenomena can be discerned from the spanwise space-time plot where there is a 'coupling' at the bottom of the cavity near $z/b = 0.7$ on alternate cycles of the fundamental. This frequency is relatively weak and intermittent and not so obvious in the signal, but is seen in the CWT scalogram between $0.3 < t < 0.8$. This reveals an important aspect of the flow that without the CWT might go undetected.

The third peak on the PSD at about $St = 0.55$ is a harmonic of the fundamental associated with dual shedding phenomena occurring with each cycle. This predominantly involves the shedding of an initial vortex once the growing cavity reaches the trailing edge and another with the bulk detachment of the condensing cavity. This frequency is evident in the time series, the CWT scalogram, and the chordwise plot as indicated by the thin streaks shed each fundamental cycle (to the left) before the much thicker bulk shed cloud (to the right).

A sample time-series of the measured unsteady lift for the nuclei abundant case is shown in the top plot of figure 12. The corresponding CWT scalogram and chordwise and spanwise space-time plots extracted from the high-speed imaging are shown in middle and bottom plots, respectively. For the nuclei abundant case the shedding physics are significantly altered due to the high concentration of continuously activated nuclei. The fundamental frequency of the bulk shedding is about $St = 0.15$, corresponding to the first peak in the PSD (figure 10). This shedding is approximately two-dimensional, occurring over the full hydrofoil span, and is about

1.8 times slower than the large-scale shedding for the nuclei deplete case. The fundamental is clearly evident in the time series, the CWT scalogram and both space-time plots.

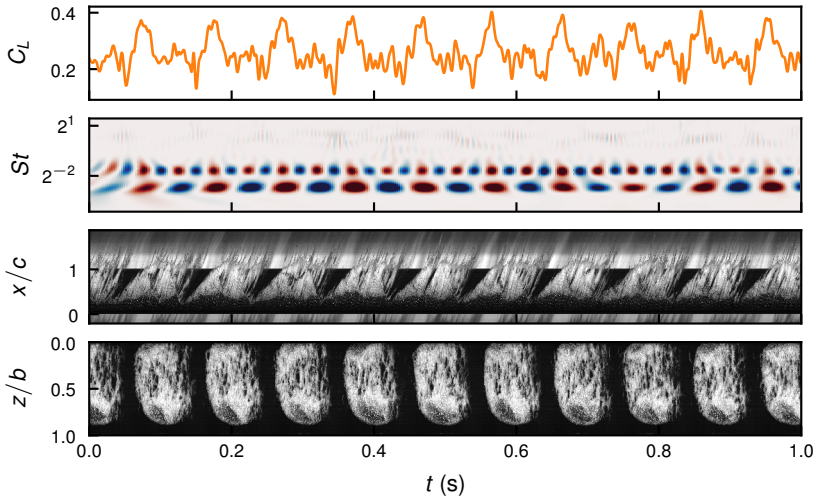

Figure 12. In the top row is the time history of the lift signal. The second figure is the real value of the Morlet wavelet transform. The bottom two figures are space-time plots at $z/b = \frac{1}{2}$ and $x/c = \frac{5}{6}$ respectively, showing the cavity extent as it varies in time.

The second peak in the PSD is a harmonic of the fundamental (about $St = 0.3$) and can be shown to be associated with the propagation of the first of two shockwaves each cycle. The first shockwave forms once the growing cavity reaches the trailing edge. This shockwave propagates upstream but loses strength and speed, stalling before reaching the cavity leading edge. Shortly after this another shockwave forms that travels upstream with greater strength and velocity, causing large scale condensation with subsequent near-two-dimensional re-growth along the hydrofoil span. The passage of the first shockwave is indicated in the chordwise space-time plot by the streakiness that occurs midway through each fundamental cycle.

6. Spectra and shedding modes of cavitation about a sphere

Canonical flows are of particular interest in basic cavitation research. One such flow is that about a sphere which has been extensively studied in single-phase flow and recently, as discussed earlier, for cavitating flow [22,23] where the CWT has been used to analyse spectral content and physical modes. This flow has the advantages of being free from wall effects in tunnels, the simple geometry can be relatively easily meshed for comparative computational studies and due to the large internal volume instrumentation can be incorporated internally. Cavitation about the sphere exhibits a range of the phenomena that are of vital interest in the field ranging from complex surface and free nucleation, surface tension/energy effects, laminar to turbulent transition and interfacial effects associated with separated boundary layers overlying cavity detachment and large scale shedding coupled with shockwave formation.

The experimental setup devised for testing of a cavitating sphere in the CRL water tunnel is shown in figure 13. A 0.15 m diameter sphere is sting-mounted on the centre-axis of the test section. The model has an interchangeable front section extending 120° on which the cavitation forms and detaches. This permits the testing of models with differing surface energy and micro-topography and for the work presented here is manufactured from polyvinyl chloride (hydrophilic) finished to 0.8 µm surface roughness. The rear section is manufactured

from stainless steel and contains two 3 mm diameter dynamic pressure sensors (PCB 105C02) located 125° from the sphere streamwise axis on the equator. High-speed images (LaVision HighSpeedStar8) were acquired on a horizontal axis from the near side simultaneously with both pressure sensors at a rate of 7 kHz for 3 s. Additional longer time series were also recorded from the surface sensors at 2^{10} Hz for 2^8 s. All data were taken at a $Re = 1.5 \times 10^6$ based on the sphere diameter, $\sigma = 0.8$ and the dissolved $O_2 = 3.3$ ppm. No nuclei were injected for these experiments. The naturally occurring background nuclei population in the tunnel have been measured using a CSM, as described above (figure 5). The very largest of these are responsible for the initial inception but are far too sparse to play a role in the high-frequency shedding and re-nucleation dynamics observed. Experiments have shown these are most likely provided by microbubbles trapped in surface viscous layers from previously shed/condensed cavities.

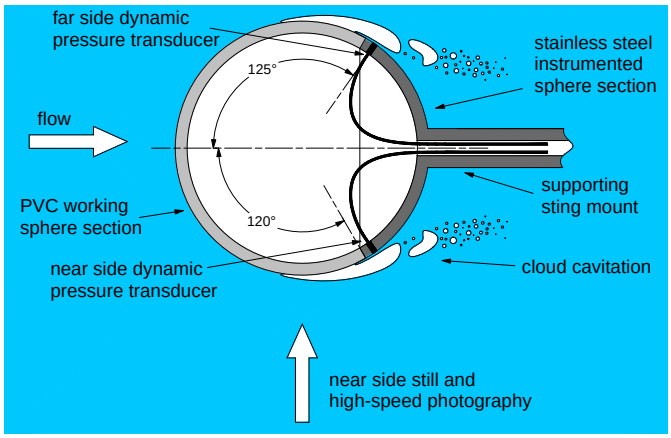

Figure 13. Cross-sectional plan view of the sphere assembly located on the streamwise axis of the water tunnel test section. Surface dynamic pressure and high-speed photography were measured simultaneously to investigate spectral content and shedding modes of the cloud cavitation. High-speed and still photography were taken horizontally from the side as indicated

It has been shown in recent studies [22,23] that cavitation about a sphere at high Reynolds numbers ranges from short stable cavities just after inception to energetic shedding at intermediate cavitation numbers before transitioning to supercavitation at low values where shedding ceases. The breakup and condensation of the short cavities just after inception are modulated by small-scale Kelvin-Helmholtz instabilities in the overlying separating laminar boundary layer. At intermediate σ values cavity lengths become sufficient for large-scale instabilities and shedding to develop, as shown in figure 14. A sample of the high-speed photography for $\sigma = 0.8$ is provided in ESM4. This shedding is predominantly bi-modal attributed to axisymmetric and asymmetric modes. This bimodal shedding occurs in attached (high σ) and detached (low σ) regimes. Although predominantly bi-modal, three modes have been identified with the onset of shedding in the attached regime at $\sigma = 0.8$.

The PSD of the near-side surface-pressure measurement for $\sigma = 0.8$ derived from the Welch estimate and the CWT using the Morlet wavelet with several non-dimensional frequencies, are shown in figure 15. The Welch estimate of the PSD shows three spectral peaks whereas the CWT using the typical non-dimensional frequency of 6 [62] shows only two. Examination of the CWT scalogram (figure 16) and the simultaneous high-speed imaging show the third mode to be physical, despite this not being apparent from the global CWT PSD. Using higher values of the non-dimensional frequency resolves the third peak (figure 15) but does come at the expense of temporal information [33].

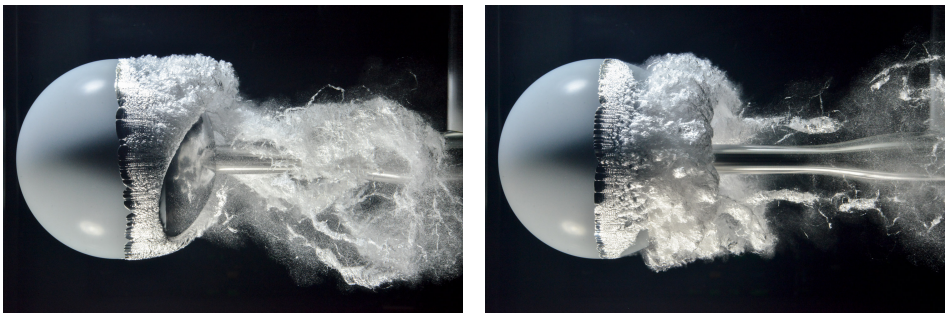

Figure 14. Side-on photographs of the cavitation about a sphere at $\sigma = 0.80$. The left-hand image shows asymmetric cavity shedding, while the structures are axisymmetric in the right-hand plot.

CWT scalograms of the short time series data for the pressure measurements either side of the sphere are shown in figure 16. The three horizontal lines indicate the three peak frequencies in the Welch PSD. The first vertical line indicates out-of-phase behaviour between the two pressures at the first frequency and second vertical line indicates in-phase behaviour for the second frequency. All three frequencies can be examined in more detail from consideration of local extracts of the time series which follows.

Local extracts from the surface-pressure time-series and corresponding CWT scalograms (using both the Morlet and DOG2 wavelets) and streamwise space-time plots from high-speed imaging above the near-side surface sensor are shown in figure 17. All these data show each of the three modes to be highly periodic but sequentially intermittent. The CWT scalograms show the third mode to be the most intermittent. The lack of resolution of the third peak in the PSD is most likely attributable to this intermittency and the lack of frequency domain resolution for the CWT PSD. This is an interesting outcome showing the complementarity of the FT and CWT for analysis of intermittent phenomena.

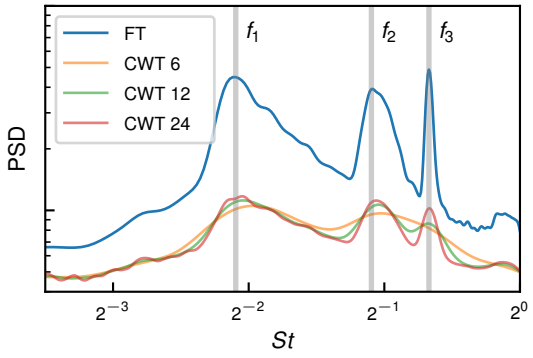

Figure 15. PSD of sphere surface pressure at σ = 0.80 derived using the FT (Welch) and the CWT using a Morlet wavelet with several non-dimensional frequencies. The FT identifies three peaks, while the third peak is only resolved with the CWT if the non-dimensional frequency is greater than the typical value of 6.

These data only provide local spatial information of spectral content, providing no insights into the global modes associated with each peak. Analysis of the global frequency content of the high-speed imaging including both amplitude and phase information and using Singular Value Decomposition has shown that f_1 and f_2 correspond to asymmetric and axisymmetric modes

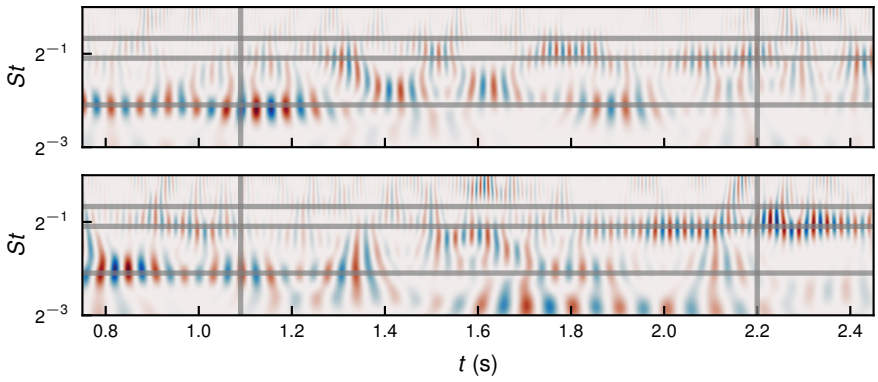

Figure 16. Real value of the CWT for the near (top) and far (bottom) pressure taps. The three horizontal lines are the three peak frequencies from f_1 to f_3 ascending. The vertical lines are guides to highlight events that are out of phase (f_1 at the left-hand vertical line), or in-phase (f_2 at the right-hand vertical line).

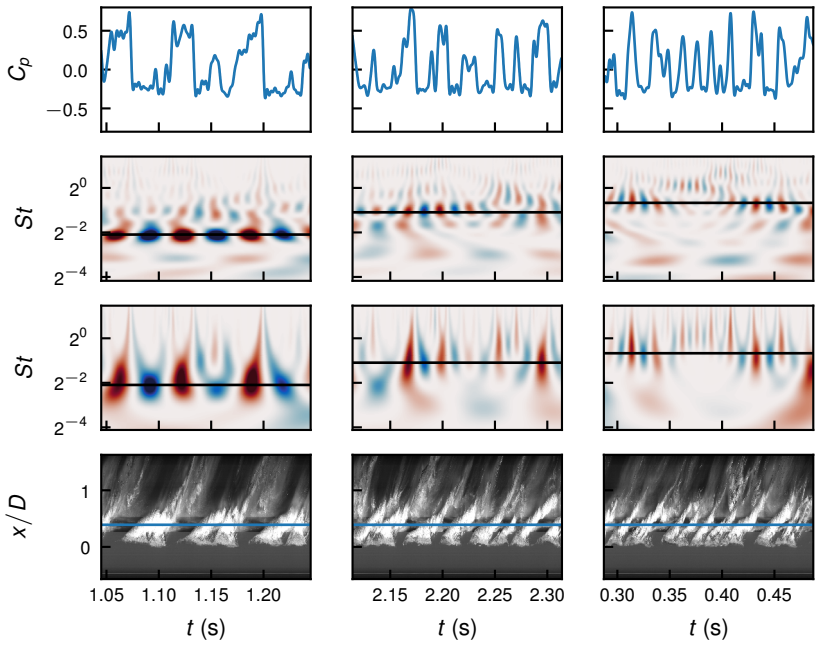

Figure 17. Sample time series of the pressure coefficient on the surface of a cavitating sphere. These time series were selected to exemplify when each of the three different frequencies, f_1 (left), f_2 (centre), and f_3 (right) were dominant. The filled contours in rows two and three are the real values of the Morlet and DOG2 wavelet transforms, respectively, and the horizontal lines indicate the frequencies of interest. The spatio-temporal map of cloud cavity position is given in the bottom row, where the horizontal line indicates the downstream location of the pressure tap.

respectively [63]. Further evidence or confirmation of this observation can be gained from the Cross Wavelet Transform (XWT) [33,64] of the simultaneous surface-pressure measurements from each side of the sphere. This has been carried out for data taken at $\sigma = 0.75$ where only the first two modes are present. A sample of the two long time-series surface-pressure measurements, the

corresponding XWT scalogram (DOG2 wavelet) and the Cross Spectral Density (XSD) from the entire record are shown in figure 18. The amplitude of the scalogram shows in-phase (positive, red) and out-of-phase (negative, blue) correlation. The XSD shows the low frequency to be correlated and out-of-phase (negative) and a maximum (in-phase) at high frequency. These frequencies are equivalent to the first two spectral peaks in the PSD shown in figure 15, confirming that the first mode is globally asymmetric and the second is axisymmetric. It is interesting to note that the second peak (axisymmetric mode) in the XSD is about twice the amplitude of the first. However there is also potential for bias due to the limited nature of the data sample with the pressures only being measured at two locations 180 $^\circ$ apart. For the axisymmetric mode, all events will be in-phase regardless of where the measurement is taken, and as such strong correlation can be expected. Whereas for the asymmetric mode there will be no preferred plane of symmetry, as the geometry is axisymmetric, so that limited out-of-phase correlation could be expected. To make more definitive observations on these aspects however requires further investigation.

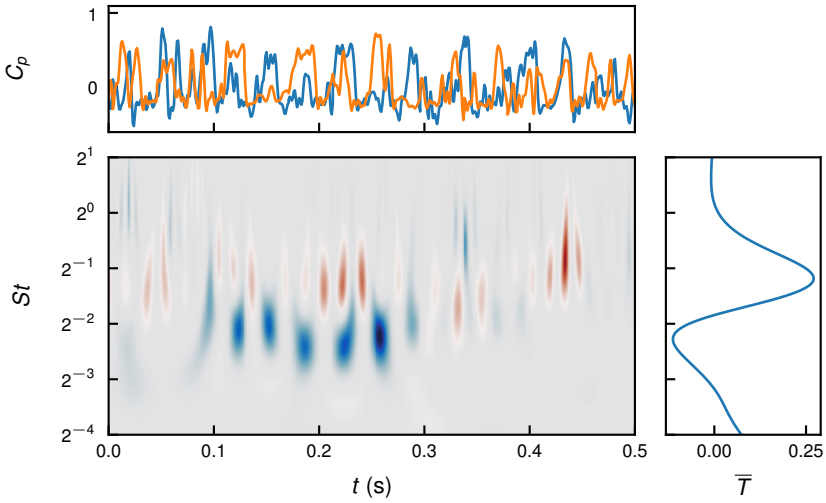

Figure 18. Time series of the pressure coefficient on the surface of a cavitating sphere for σ = 0.75 where only two modes are present. The two pressure taps are located on opposite sides of the sphere. The cross-wavelet transform, here using the DOG2 wavelet, allows for an easy comparison of the phasing of different temporal events, and the coherence between the two signals. The XSD indicates that the first frequency is out-of-phase and the second frequency to be in-phase.

A similar analysis can also be applied to the two pressure signals corresponding to the short time series data presented in figure 17 for all of the spectral peaks shown in the Welch PSD. The pressure signals from both side of the sphere and corresponding XWT scalograms and XSD are shown in figure 19. These data show results that concur with those above for the fist two modes consistent with asymmetric and axisymmetric global modes. The XWT scalogram and XSD for f_3 show no correlation at this frequency, suggesting that this mode is purely a local effect with no associated large-scale flow features. This raises the question of what global flow behavior does occur when this local mode is present. To answer this and other questions requires further investigation with an increased number of pressure measurement locations and at least two cameras to simultaneously image the cavitation on both sides of the sphere. It should also be noted that although the analysis of the conditionally sampled data concur with observations for the long time-series for the first two frequencies, these data are too limited to make definitive conclusions.

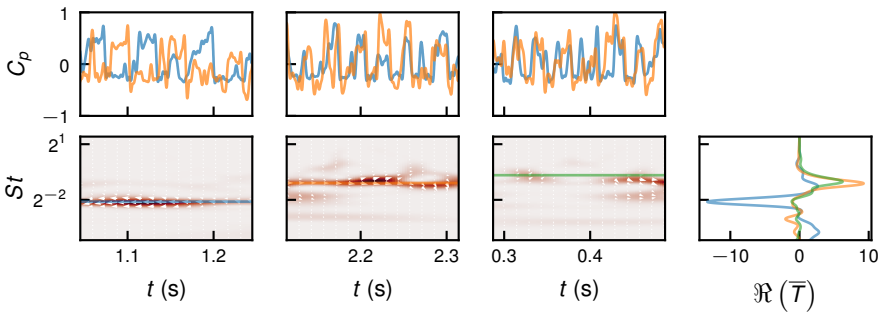

Figure 19. Pressure coefficient on the surface of a cavitating sphere for three selected time series corresponding to each of the three frequencies. The two pressure taps are located on opposite sides of the sphere. The absolute value of the Morlet cross-wavelet transform is given by the filled contours representing the coherence between the two signals at that Strouhal number. Coherence is evident for only f_1 and f_2. The overlaid arrows represent the phase difference between the two signals (in-phase signals are indicated by an arrow to the right, a $\pi/2$ phase difference is indicated by an arrow upwards). The right-most figure is a time-integral of the real part of the wavelet transform, which indicates in a broad sense whether the two signals are in phase (positive) or out-of-phase (negative).

7. Conclusions

The continuous wavelet transform has become a standard tool in the analysis of cavitating flows. It is a powerful addition to, and complements, other analysis techniques such as the classical Fourier transform and various methods of modal decomposition. It is in this combination that new insights into the complex phenomena involved in cavitating flows have been gained. Wavelets have been applied in data analysis of all aspects of cavitation ranging from nucleation at micron scales to large-scale shedding and shockwave phenomena at metre scales. In many cases the use of wavelets have provided a means to extract certain information that other techniques do not provide. This paper has only briefly presented a few examples of where wavelets have been used to identify new aspects and phenomena in cavitating flows and the reader is referred to the literature for more detail. Most of the applications presented here involved one-dimensional data with one example of two-dimensional data using the cross wavelet transform. With ever-increasing computer power, wavelets will undoubtedly find new applications in higher dimensional data sets where at present only the Fast Fourier Transform is applied. Such an example is in the modal analysis of high-speed imaging using single and multiple cameras for two- and three-dimensional imaging.

Acknowledgements. The authors acknowledge the support of the University of Tasmania, the Australian Defence Science and Technology Group and the US Office of Naval Research (Dr. Ki-Han Kim, Program Officer) and ONR Global (Dr. Woei-Min Lin) through NICOP S&T Grant no. N62909-15-1-2019. Wavelet software was provided by C. Torrence and G. Compo [62], and is available at: http://paos.colorado.edu/research/wavelets/.

References

1. Farge M. 1992 Wavelet transforms and their applications to turbulence. *Annual Review of Fluid Mechanics* **24**, 395–457. (doi:10.1146/annurev.fl.24.010192.002143)
2. Schneider K, Vasilyev OV. 2010 Wavelet methods in computational fluid dynamics. *Annual Review of Fluid Mechanics* **42**, 473–503. (doi:10.1146/annurev-fluid-121108-145637)

3. Grossmann A, Morlet J. 1984 Decomposition of hardy functions into square integrable wavelets of constant shape.
SIAM Journal on Mathematical Analysis **15**, 723–736.
(doi:10.1137/0515056)
4. Farge M, Rabreau G. 1988 Wavelet transform to detect and analyze coherent structures in two-dimensional turbulent flows.
Comptes Rendus de l'Académie des Sciences - Series II **307**, 1479–1486.
5. Farge M, Guezennec Y, Ho CM, Meneveau C. 1990 Continuous wavelet analysis of coherent structures.
In *Center for Tubulence Research - 1990 Summer Program*, pp. 331–348.
6. Meneveau C. 1991 Analysis of turbulence in the orthonormal wavelet representation.
Journal of Fluid Mechanics **232**, 469–520.
(doi:10.1017/S0022112091003786)
7. Baars WJ, Talluru KM, Hutchins N, Marusic I. 2015 Wavelet analysis of wall turbulence to study large-scale modulation of small scales.
Experiments in Fluids **56**, 188.
(doi:10.1007/s00348-015-2058-8)
8. Baars WJ, Hutchins N, Marusic I. 2017 Reynolds number trend of hierarchies and scale interactions in turbulent boundary layers.
Philosophical transactions of the Royal Society of London. Series A **375**, 20160077.
(doi:10.1098/rsta.2016.0077)
9. Bowles RI. 2000 Transition to turbulent flow in aerodynamics.
Philosophical transactions of the Royal Society of London. Series A: Mathematical, physical, and engineering sciences **358**, 245–260.
(doi:10.1098/rsta.2000.0530)
10. Simoni D, Lengani D, Guida R. 2016 A wavelet-based intermittency detection technique from piv investigations in transitional boundary layers.
Experiments in Fluids **57**, 145.
(doi:10.1007/s00348-016-2231-8)
11. Bosschers J. 2009 Investigation of hull pressure fluctuations generated by cavitating vortices.
In *1st International Symposium on Marine Propulsors (smp'09)*. Trondheim, Norway.
12. Baars WJ, Tinney CE. 2013 Transient wall pressures in an overexpanded and large area ratio nozzle.
Experiments in Fluids **54**, 1468.
(doi:10.1007/s00348-013-1468-8)
13. Van Blitterswyk J, Rocha J. 2017 An experimental study of the wall-pressure fluctuations beneath low reynolds number turbulent boundary layers.
Journal of the Acoustical Society of America **141**, 1257.
(doi:10.1121/1.4976341)
14. Cavalieri AV, Daviller G, Comte P, Jordan P, Tadmor G, Gervais Y. 2011 Using large eddy simulation to explore sound-source mechanisms in jets.
Journal of Sound and Vibration **330**, 4098–4113.
(doi:10.1016/j.jsv.2011.04.018)
15. Felli M, Grizzi S, Falchi M. 2014 A novel approach for the isolation of the sound and pseudo-sound contributions from near-field pressure fluctuation measurements: analysis of the hydroacoustic and hydrodynamic perturbation in a propeller-rudder system.
Experiments in Fluids **55**, 1651.
(doi:10.1007/s00348-013-1651-y)
16. Cierpka C, Weier T, Gerbeth G. 2008 Evolution of vortex structures in an electromagnetically excited separated flow.
Experiments in Fluids **45**, 943–953.
(doi:10.1007/s00348-008-0512-6)
17. Kim YH, Cierpka C, Wereley S. 2011 Flow field around a vibrating cantilever: coherent structure eduction by continuous wavelet transform and proper orthogonal decomposition.
Journal of Fluid Mechanics **669**, 584–606.
(doi:10.1017/S0022112010005318)
18. Wang L, Hu R, Zhang J, Ma Y. 2015 On the vortex detection method using continuous wavelet transform with application to propeller wake analysis.

Mathematical Problems in Engineering **2015**, 242917.
(doi:10.1155/2015/242917)
19. Ruppert-Felsot J, Farge M, Petitjeans P. 2009 Wavelet tools to study intermittency: application to vortex bursting.
Journal of Fluid Mechanics **636**, 427—453.
(doi:10.1017/S0022112009008003)
20. Parkin DJ, Thompson M, Sheridan J. 2014 Numerical analysis of bluff body wakes under periodic open-loop control.
Journal of Fluid Mechanics **739**, 94–123.
(doi:10.1017/jfm.2013.618)
21. Kjeldsen M, Arndt RE. 2001 Joint time frequency analysis techniques: A study of transitional dynamics in sheet/cloud cavitation.
In *4th International Symposium on Cavitation (CAV2001)*. California Institute of Technology.
22. Brandner P, Walker G, Niekamp P, Anderson B. 2010 An experimental investigation of cloud cavitation about a sphere.
Journal of Fluid Mechanics **656**, 147–176.
(doi:10.1017/S0022112010001072)
23. de Graaf KL, Brandner PA, Pearce BW. 2017 Spectral content of cloud cavitation about a sphere.
Journal of Fluid Mechanics **812**, R1.
(doi:10.1017/jfm.2016.819)
24. Gopalan S, Katz J, Liu HL. 2001 Tip leakage cavitation, associated bubble dynamics, noise, flow structure and effect of tip gap size.
In *4th International Symposium on Cavitation (CAV2001)*. California Institute of Technology.
25. He Y, Liu Y. 2011 Experimental research into time–frequency characteristics of cavitation noise using wavelet scalogram.
Applied Acoustics **72**, 721—-731.
(doi:10.1016/j.apacoust.2011.03.008)
26. Herbertson LH, Reddy V, Manning KB, Welz JP, Fontaine AA, Deutsch S. 2006 Wavelet transforms in the analysis of mechanical heart valve cavitation.
Journal of Biomechanical Engineering **128**, 217–222.
(doi:10.1115/1.2165694)
27. Lebrun D, Allano D, Méès L, Walle F, Corbin F, Boucheron R, Fréchou D. 2011 Size measurement of bubbles in a cavitation tunnel by digital in-line holography.
Applied Optics **50**, H1–H9.
(doi:10.1364/AO.50.0000H1)
28. de Graaf K, Brandner P, Penesis I. 2014 The pressure field generated by a seismic airgun.
Experimental Thermal and Fluid Science **55**, 239—-249.
(doi:10.1016/j.expthermflusci.2014.02.025)
29. Brandner PA, Henderson A, de Graaf K, Pearce BW. 2015 Bubble breakup in a turbulent shear layer.
Journal of Physics: Conference Series **656**, 012015.
(doi:10.1088/1742-6596/656/1/012015)
30. Taira K, Brunton SL, Dawson STM, Rowley CW, Colonius T, McKeon BJ, Schmidt OT, Gordeyev S, Theofilis V, Ukeiley LS. 2017 Modal analysis of fluid flows: An overview.
AIAA Journal **55**, 4013–4041.
(doi:10.2514/1.J056060)
31. Prothin S, Billard JY, Djeridi H. 2016 Image processing using proper orthogonal and dynamic mode decompositions for the study of cavitation developing on a naca0015 foil.
Experiments in Fluids **57**, 157.
(doi:10.1007/s00348-016-2246-1)
32. Barbaca L, Pearce BW, Brandner PA, Ganesh H, Ceccio SL. 2018 On the unsteady behaviour of cavity flow over a 2-d wall-mounted fence.
Under consideration for publishing in *Journal of Fluid Mechanics* .
33. Addison PS. 2016 *The Illustrated Wavelet Transform Handbook: Introductory Theory and Applications in Science, Engineering, Medicine and Finance*.
CRC Press, 2nd edition.
34. Brandner PA, Pearce BW, de Graaf K. 2015 Cavitation about a jet in crossflow.

Journal of Fluid Mechanics **768**, 141–174.
(doi:10.1017/jfm.2015.73)
35. Brennen CE. 1995 *Cavitation and Bubble Dynamics*.
Oxford University Press.
36. Franc JP, Michel JM. 2004 *Fundamentals of Cavitation*.
Dordrecht: Kluwer Academic Publishers.
37. Medwin H. 1970 In situ acoustic measurements of bubble populations in coastal ocean waters.
Journal of Geophysical Research **75**, 599–611.
(doi:10.1029/JC075i003p00599)
38. Medwin H. 1977 In situ acoustic measurements of microbubbles at sea.
Journal of Geophysical Research **82**, 971—-976.
(doi:10.1029/JC082i006p00971)
39. O'Hern TJ. 1987 *Cavitation inception scale effects : I. Nuclei distributions in natural waters. II. Cavitation inception in a turbulent shear flow*.
PhD thesis, California Institute of Technology.
40. Gindroz B. 1995 Propeller cavitation characteristics: The practical interest of nuclei measurements in test facilities and at sea.
In *Symposium on Cavitation and Gas-Liquid Flow in Fluid Machinery and Devices. FED Vol.226*, pp. 151–159. Hilton Head, South Carolina: ASME.
41. Yu H, Goldsworthy L, Brandner P, Garaniya V. 2017 Development of a compressible multiphase cavitation approach for diesel spray modelling.
Applied Mathematical Modelling **45**, 705–727.
(doi:10.1016/j.apm.2017.01.035)
42. Dular M, Griessler-Bulc T, Gutierrez-Aguirre I, Heath E, Kosjek T, Klemenc AK, Oder M, Petkovšek M, Racki N, Ravnikarc M, Šarc A, Širok B, Zupanc M, Žitnik M, Komparee B. 2016 Use of hydrodynamic cavitation in (waste)water treatment.
Ultrasonics Sonochemistry **29**, 577–588.
(doi:10.1016/j.ultsonch.2015.10.010)
43. Suslick KS, Flannigan DJ. 2008 Inside a collapsing bubble: Sonoluminescence and the conditions during cavitation.
Annual Review of Physical Chemistry **59**, 659–683.
(doi:10.1146/annurev.physchem.59.032607.093739)
44. Brennen CE. 2015 Cavitation in medicine.
Interface Focus **5**, 20150022.
45. Giosio DR, Pearce BW, Brandner PA. 2016 Influence of pressure on microbubble production rate in a confined turbulent jet.
In *20th Australasian Fluid Mechanics Conference*, p. Paper 717. Perth, Australia: AFMS.
46. Venning JA, De Vincentis S, Pearce BW, Brandner PA. 2016 Microbubble generation for PIV seeding.
In *20th Australasian Fluid Mechanics Conference*, p. Paper 758. Perth, Australia: AFMS.
47. van de Hulst H. 1981 *Light scattering by small particles*.
New York: Dover publications, Inc.
48. Damaschke N, Nobach H, Nonn TI, Semidetnov N, Tropea C. 2005 Multi-dimensional particle sizing techniques.
Experiments in Fluids **39**, 336–350.
(doi:10.1007/s00348-005-1009-1)
49. Oldenziel D. 1982 A new instrument in cavitation research: the cavitation susceptibility meter.
Journal of Fluids Engineering **104**, 136–141.
(doi:10.1115/1.3241790)
50. Khoo MT, Venning JA, Pearce BW, Brandner PA, Lecoffre Y. 2016 Development of a cavitation susceptibility meter for nuclei size distribution measurements.
In *20th Australasian Fluid Mechanics Conference*, p. Paper 662a. Perth, Australia: AFMS.
51. Venning JA, Khoo MT, Pearce BW, Brandner PA. 2018 Background nuclei measurements and implications for cavitation inception in hydrodynamic test facilities.
Experiments in Fluids **59**, 71.
(doi:10.1007/s00348-018-2520-5)
52. Castro AM, Carrica PM. 2013 Bubble size distribution prediction for large-scale ship flows: Model evaluation and numerical issues.

International Journal of Multiphase Flow **57**, 131–150.
(doi:10.1016/j.ijmultiphaseflow.2013.08.001)
53. Castro AM, Li J, Carrica PM. 2016 A mechanistic model of bubble entrainment in turbulent free surface flows.
International Journal of Multiphase Flow **86**, 35–55.
(doi:10.1016/j.ijmultiphaseflow.2016.07.005)
54. Liao Y, Lucas D. 2009 A literature review of theoretical models for drop and bubble breakup in turbulent dispersions.
Chemical Engineering Science **64**, 3389–3406.
(doi:10.1016/j.ces.2009.04.026)
55. Liao Y, Lucas D. 2010 A literature review on mechanisms and models for the coalescence process of fluid particles.
Chemical Engineering Science **65**, 2851–2864.
(doi:10.1016/j.ces.2010.02.020)
56. Deane GB, Stokes MD. 2002 Scale dependence of bubble creation mechanisms in breaking waves.
Nature **418**, 839–844.
(doi:10.1038/nature00967)
57. Churnside JH. 2010 Lidar signature from bubbles in the sea.
Optics Express **18**, 8294–8299.
(doi:10.1364/OE.18.008294)
58. Deane GB, Stokes MD. 2006 The acoustic signature of bubbles fragmenting in sheared flow.
Journal of the Acoustical Society of America **120**, EL84–EL89.
(doi:10.1121/1.2364466)
59. Kouzoubov A, Wood S, Ellem R. 2014 Acoustic imaging of surface ship wakes.
In *43rd International Congress on Noise Control Engineering (Inter Noise 2014)*, p. Paper 544. Melbourne, Australia.
60. Leighton T, Walton A. 1987 An experimental study of the sound emitted from gas bubbles in a liquid.
European Journal of Physics **8**, 98–104.
(doi:10.1088/0143-0807/8/2/005)
61. Venning J, Smith S, Brandner P, Giosio D, Pearce B. 2017 The influence of nuclei content on cloud cavitation about a hydrofoil.
In *17th International Symposium on Transport Phenomena and Dynamics of Rotating Machinery (ISROMAC17)*. Maui, Hawaii, U.S.A.
62. Torrence C, Compo GP. 1998 A practical guide to wavelet analysis.
Bulletin of the American Meteorological Society **79**, 61–78.
(doi:10.1175/1520-0477(1998)079<0061:APGTWA>2.0.CO;2)
63. Venning JA, Giosio DR, Pearce BW, Brandner PA. 2018 Global mode visualisation in cavitating flows.
In *10th International Symposium on Cavitation (Cav2018)*. Baltimore, Maryland, USA.
64. Grinsted A, Moore JC, Jevrejeva S. 2004 Application of the cross wavelet transform and wavelet coherence to geophysical time series.
Nonlinear Processes in Geophysics **11**, 561–566.
(doi:10.5194/npg-11-561-2004)